Moiré excitons in defective van der Waals heterostructures

Hongli Guo[a], Xu Zhang[a], and Gang Lu[a,1]

[a]Department of Physics and Astronomy, California State University, Northridge, CA 91330-8268

Excitons can be trapped by moiré potentials in van der Waals (vdW) heterostructures, forming ordered arrays of quantum dots. Excitons can also be trapped by defect potentials as single photon emitters. While the moiré and defect potentials in vdW heterostructures have been studied separately, their interplay remains largely unexplored. Here, we perform first-principles calculations to elucidate the interplay of the two potentials in determining the optoelectronic properties of twisted MoS_2/WS_2 heterobilayers. The binding energy, charge density, localization, and hybridization of the moiré excitons can be modulated by the competition and cooperation of the two potentials. Their interplay can also be tuned by vertical electric fields, which can either de-trap the excitons or strongly localize them. One can further tailor the interplay of the two potentials via defect engineering to create one-dimensional exciton lattices with tunable orientations. Our work establishes defect engineering as a promising strategy to realize on-demand optoelectronic responses.

moiré excitons | vdW heterostructures | defect engineering | TDDFT

Moiré superlattices formed by stacking two-dimensional (2D) materials with a small angular or lattice mismatch provide a powerful and versatile platform for engineering quantum states of matter (1–7). Recent observations of ordered arrays of zero-dimensional (0D) (8–10) and one-dimensional (1D) (11) moiré excitons in transition metal dichalcogenide (TMD) heterostructures have injected more excitement into this burgeoning field. Confined by the moiré potential, these localized, long-lived, and valley-polarized interlayer excitons have garnered tremendous interest, from fundamental science, such as Bose–Einstein condensation (7) to novel applications, such as single-photon emitters in quantum information and optoelectronic devices (12, 13).

Defects are inevitable in materials and can strongly influence materials properties and device performance (14, 15); most notably, defects can trap excitons and charge carriers. A number of theoretical and experimental studies have been carried out to identify prolific defects in TMDs and particularly to examine defect-bound excitons (16–19). Although these studies provided crucial insight into the defect physics, they focused exclusively on TMD monolayers, in the absence of moiré potentials. Thus, how defects may influence moiré excitons is largely unknown; in fact, it is not clear (and indeed surprising) how moiré excitons can remain highly robust in imperfect TMD heterostructures (20). Since both the defect and moiré potentials can trap excitons, their interplay—competition and cooperation—in modulating the excitonic properties in van der Waals (vdW) heterostructures is of significant interest, but yet unexplored.

In this work, we perform first-principles calculations to elucidate the interplay of the defect and moiré potentials in tailoring the excitonic properties in twisted vdW heterostructures of MoS_2/WS_2. The conventional first-principles approach to capture excitonic effect in semiconductors is GW/Bethe–Salpeter equation (GW-BSE) method (21–23) based on many-body perturbation theory. However, the GW-BSE method is prohibitively expensive for modeling moiré excitons owing to large moiré supercells. To circumvent the problem, we employed an alternative first-principles method that can provide a reliable description of the excitonic effect with substantially lower computational cost (24–28). This method is based on time-independent and time-dependent density functional theory (29, 30) with optimally tuned, screened, and range-separated hybrid exchange-correlation functionals (31–35); the former is used to predict quasiparticle energy levels and the latter for excitonic properties (details are in *Methods*). Using this method, we explore how the interplay of the defect and moiré potentials could modulate the binding energy, charge density, spatial localization, and hybridization of excitons in twisted MoS_2/WS_2 heterobilayers. The interplay can be tuned by a vertical electric field, which can either de-trap the excitons or further localize them. The interplay of the two potentials can also be tailored via defect engineering to create 1D exciton lattices with tunable orientations. Our work provides an in-depth study of defect-trapped moiré excitons in vdW heterostructures and establishes defect engineering as a promising strategy to tailor optoelectronic responses on demand.

Results

Defect-Induced Excitons in Nontwisted TMD Heterostructures. As a validation of our first-principles method, we first examine $MoSe_2$ monolayer in the presence of a single Se vacancy (Se_v) for which previous GW-BSE and experimental results are available for comparisons. The quasiparticle bandgap of the pristine monolayer is 2.30 eV and the Se vacancy introduces a defect level 0.56 eV below the conduction band minimum (CBM). The binding energy of the lowest energy exciton in the pristine monolayer is 0.51 eV, which is 20 meV smaller than that of the defect-induced exciton (0.53 eV). All these quantities are in good agreement with previous GW-BSE (16) and experimental (36) results, which demonstrates

Significance

Defects are inevitable in van der Waals (vdW) materials, but their role on moiré excitons remains unknown. While both moiré and defect potentials can trap excitons in twisted vdW heterostructures, their interplay has not been explored thus far. In this work, we perform first-principles simulations to elucidate the interplay of the defect and moiré potentials in tailoring the excitonic properties in twisted vdW heterostructures. Our work provides an in-depth study of defect-trapped moiré excitons in vdW heterostructures and establishes defect engineering as a promising strategy to tailor optoelectronic responses on demand.

the validity of our first-principles method. More details can be found in *SI Appendix*, Fig. S1.

We next turn to lattice aligned MoS_2/WS_2 heterobilayers (twist angle $\theta = 0°$) in the presence of vacancy defects. In the absence of angular misalignment or lattice mismatch (the lattice constant difference between MoS_2 and WS_2 is negligible), there is no moiré potential in these heterobilayers. In our first-principles simulations, a $\sqrt{271} \times \sqrt{271}$ supercell is adopted containing 1,626 atoms, which yields a reasonable vacancy concentration at 4.18×10^{12} cm^{-2}. A number of neutral vacancies, including S vacancy (S_v) in MoS_2 ($S_v@MoS_2$) and WS_2 ($S_v@WS_2$) as well as Mo and W vacancies (Mo_v and W_v) are considered in the present work.

In Fig. 1, we display the quasiparticle energy levels and the charge density of the lowest energy exciton in the perfect and defective nontwisted MoS_2/WS_2 heterobilayers. All these defects are found to produce in-gap states and localized excitons. Specifically, S vacancy introduces a pair of defect levels below the CBM, independent of the vacancy location (WS_2 or MoS_2). As a result, the lowest exciton in both cases ($S_v@MoS_2$ and $S_v@WS_2$) involves an optical transition between the valence band maximum (VBM) and the defect level. When S_v is in MoS_2 layer, the electron is trapped at the vacancy while the hole spreads over WS_2 layer; thus, the exciton maintains its interlayer feature of the pristine heterostructure. On the other hand, when S_v is in WS_2 layer, both the electron and the hole reside in WS_2, forming an intralayer exciton. In contrast to S_v, each metal vacancy (Mo_v or W_v) creates three deep levels in the bandgap and one occupied level in the valence band; the lowest energy exciton thus corresponds to an optical transition between the occupied defect level and the in-gap defect level. Hence, both the electron and the hole are localized at the metal vacancy, yielding a defect-bound intralayer exciton.

In Tables 1 and 2, we summarize the quasiparticle bandgap, optical gap, and exciton binding energy for the five nontwisted heterobilayers. It is found that as the exciton becomes more localized, its binding energy increases accordingly. In particular, the metal vacancies yield more strongly bound excitons than S vacancies, and the intralayer exciton has a higher binding energy than the interlayer counterpart. A recent GW-BSE calculation predicted the exciton binding energy for a Se vacancy in monolayer $MoSe_2$ as 600 meV (16), which is 50 meV higher than that of the A exciton in perfect $MoSe_2$ (36). Thus, Se vacancy increases exciton binding by 50 meV, which is similar to the increase (50–70 meV) by S_v in MoS_2/WS_2. Because S vacancy has the lower formation energy than Mo and W vacancies and can be introduced to the materials by high-temperature annealing and electron-beam irradiation (17,

Table 1. Quasiparticle (QP) gap, optical gap, and exciton binding energy for the nontwisted heterobilayers with different vacancies

Nontwisted	Perfect	$S_v@Mo$	$S_v@W$	Mo_v	W_v
QP gap, eV	2.00	1.625	1.845	1.089	1.094
Optical gap, eV	1.794	1.377	1.566	0.652	0.704
Binding energy, meV	207	248	279	437	390

18, 37), we will focus on S vacancies in the remaining of the paper.

Defect-Induced Excitons in Twisted TMD Heterostructures. In the following, we examine moiré excitons in twisted MoS_2/WS_2 heterobilayers in the presence of S vacancies. In Fig. 2 *A* and *B*, we display the unit cells of two moiré superlattices formed by a relative twist between MoS_2 and WS_2 monolayers with angles $\theta = 3.5°$ and $\theta = 56.5°$, respectively; the two unit cells have the identical lattice constant (5.25 nm) and number of atoms (1,626). In both moiré superlattices, there are three local atomic stacking motifs, labeled by A, B, and C, that preserve the threefold rotational symmetry and are commonly used to characterize the moiré potentials in TMD heterostructures. For $\theta = 3.5°$ ($\theta = 56.5°$), these motifs are often referred to as R-type (H-type) stacking.

In contrast to nontwisted heterostructures, there are two types of confining potentials in a defective and twisted heterostructure, i.e., defect potential and moiré potential. The former is centered at defects, while the latter is centered at high symmetry points of a moiré superlattice. Depending on the nature of the defect, the defect potential can trap either electron or hole. However, owing to strong exciton binding in 2D TMDs, the electron and the hole are expected to localize at the same defect in the absence of a moiré potential, as demonstrated above. At the same time, excitons can also be confined by moiré potentials, as shown by numerous experimental and theoretical studies (8–10, 28, 38, 39). In particular, we have revealed that the motifs B and C sit at the bottom of the moiré potential, while the motif A is at the top of the potential in twisted MoS_2/WS_2 heterobilayers (28). Thus, depending on the position of the defect, the two confining potentials could either cooperate or compete in trapping excitons and modulating their properties. Furthermore, the potentials and their interplay can be tuned by external means, such as electric field, pressure, and strain.
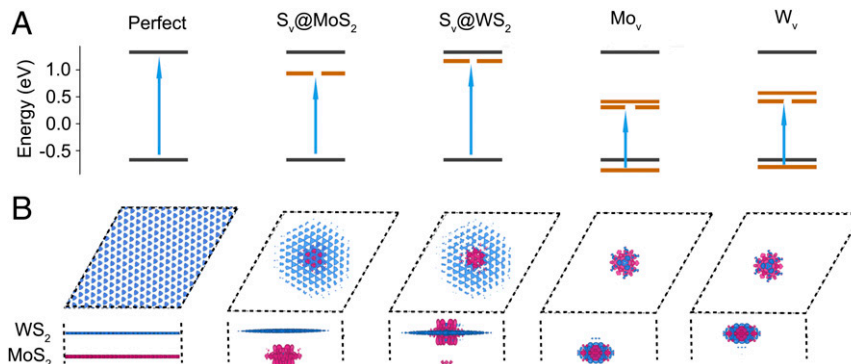

Fig. 1. (*A*) The schematic band diagrams of the heterobilayer in the absence and presence of defects. A single S vacancy is introduced in either MoS_2 ($S_v@MoS_2$) or WS_2 layer ($S_v@WS_2$); a single Mo vacancy (Mo_v) or W vacancy (W_v) is also considered. The CBM and VBM of the perfect heterostructure are represented by the black lines, while the defect levels are shown by the orange lines. The arrow indicates the lowest energy excitation (exciton). (*B*) The charge density of the lowest energy exciton with the red and blue color representing the charge densities of electron and hole, respectively; both the top and side views are displayed. The computational unit cell is indicated by the dashed box. All iso-surface value is set at 0.0001 e/Å^3.

Table 2. Exciton binding energy in the twisted heterobilayers with $\theta = 3.5°$ and $\theta = 56.5°$ with single S vacancy introduced in MoS$_2$ or WS$_2$ layer and in different positions

Twisted	Perfect	S$_v$@Mo@A	S$_v$@Mo@B	S$_v$@Mo@C	S$_v$@W@A	S$_v$@W@B	S$_v$@W@C
$\theta = 3.5°$, meV	207	184	222	218	184	266	286
$\theta = 56.5°$, meV	194	176	190	258	180	237	325

The notation S$_v$@Mo@A (or B, C) indicates that the S vacancy resides at the high symmetry point A (or B, C) in MoS$_2$ layer. The high symmetry points A, B, and C are defined in Fig. 2.

To illustrate the interplay of the two potentials in tuning the excitonic properties, we focus on the twisted MoS$_2$/WS$_2$ heterobilayers ($\theta = 3.5°$); S vacancy is introduced at the three high symmetry points (A, B, and C) in either MoS$_2$ or WS$_2$ layer. The vacancy formation energy differs slightly (~20 meV) among the high symmetry points for both S$_v$@MoS$_2$ and S$_v$@WS$_2$. The formation energy of S$_v$@MoS$_2$, on the other hand, is 200 meV lower than that of S$_v$@WS$_2$. Our previous work has estimated the maximum depth of the moiré potential in twisted MoS$_2$/WS$_2$ heterobilayers. It is found that the moiré potential at A is 0.26 eV higher than that at B and C, whereas the moiré potential at B is slightly higher than that at C (28). Note that 0.26 eV represents the maximum depth in all MoS$_2$/WS$_2$ heterobilayers, and the actual moiré potential depth in the heterobilayer with $\theta = 3.5°$ may be smaller. As shown in *SI Appendix*, Fig. S6, we also provide an alternative estimate for the moiré potential in the R- and H-stacking MoS$_2$/WS$_2$ heterobilayers based on the local density of states. The moiré potential is estimated as 0.18 eV for $\theta = 3.5°$ heterobilayer. In comparison, the experimental estimate
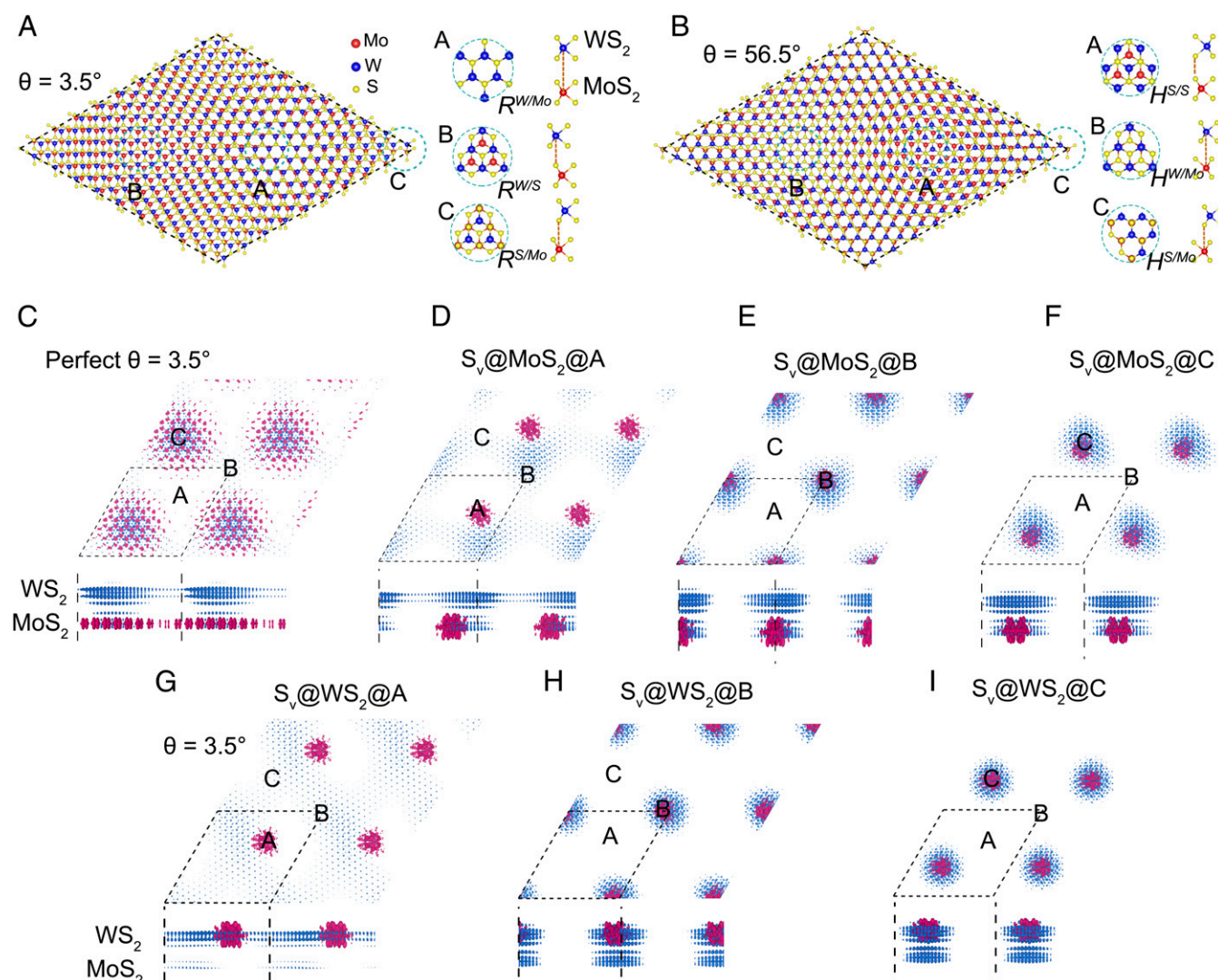

Fig. 2. The unit cell of the moiré superlattice formed by a twisted MoS$_2$/WS$_2$ heterobilayer with twist angle $\theta = 3.5°$ (*A*) and $\theta = 56.5°$ (*B*). The stacking configurations of the three local motifs, A, B, and C (dashed circles), are shown on the *Right*. (*C*) Charge density of the lowest exciton in pristine twisted MoS$_2$/WS$_2$ heterobilayer with $\theta = 3.5°$. *D–F* and *G–I* represent the charge density of the lowest exciton with a S vacancy at various high symmetry points in MoS$_2$ and WS$_2$ layer, respectively. Both the top and side views are displayed. Red and blue colors represent the charge densities of electron and hole, respectively. The unit cell of the moiré superlattice is indicated by the dashed box. All iso-surface value is set at 0.0001 e/Å^3.

Guo et al.
Moiré excitons in defective van der Waals heterostructures

PNAS | 3 of 9
https://doi.org/10.1073/pnas.2105468118

for the moiré potentials in $WSe_2/MoSe_2$ heterobilayers can reach 0.30 and 0.15 eV for the valence and conduction bands, respectively (40).

We can also estimate the depth of the defect potential by its energetic offset with respect to the CBM in the twisted heterobilayer with $\theta = 3.5°$, as shown in *SI Appendix*, Fig. S2. The depth of the defect potential for $S_v@MoS_2$ and $S_v@WS_2$ is estimated as 0.5 and 0.3 eV, respectively. Therefore, in the MoS_2/WS_2 heterobilayers, the defect potential is deeper than the moiré potential. However, in other twisted TMD heterobilayers (e.g., $WSe_2/MoSe_2$), the moiré potentials could be much deeper (40) and thus comparable to the defect potentials.

In Fig. 2 *C–I*, we present the charge density of the lowest energy exciton in the twisted MoS_2/WS_2 heterobilayers ($\theta = 3.5°$) with S vacancy at various high symmetry points in the two layers. In the absence of the defect potential, the exciton would prefer C slightly over B, but strongly disfavor A. On the other hand, in the absence of the moiré potential, the electron would be trapped at the vacancy. Because the defect potential is deeper than the moiré potential at the high symmetry points, the defect potential prevails and the electron is trapped at the vacancy, independent of the vacancy position. The hole distribution, on the other hand, depends on the position of the vacancy, which is a manifestation of the interplay between the two potentials. More specifically, when the vacancy is at C (Fig. 2 *F* and *I*) where the moiré potential is at its minimum, the two potentials cooperate to form a deeper trap for the exciton, with both electron and hole localized at C. The same scenario holds when the vacancy is at B (Fig. 2 *E* and *H*) with both electron and hole trapped at the defect. However, when the vacancy is at A (Fig. 2 *D* and *G*) where the moiré potential is at its maximum, the two potentials compete; the electron is trapped at A while the hole settles somewhere away from the high symmetry points to avoid the high moiré potential at A. Hence the competition between the two potentials partially separates the electron and the hole despite the strong exciton binding energy. The main difference between $S_v@MoS_2$ and $S_v@WS_2$ is that the lowest energy exciton retains its interlayer character in the former, but it gains more intralayer (or hybridized) character in the latter. The same competition and cooperation phenomena are also found in twisted MoS_2/WS_2 heterobilayer with $\theta = 56.5°$ and the competition and cooperation of the two potentials appear even stronger. As shown in *SI Appendix*, Fig. S3, the lowest exciton exhibits larger charge separation when the two potentials compete, and it is more localized when the two potentials cooperate. Last, we note that lattice relaxation can have significant effects on moiré potentials and moiré excitons. We have examined the lattice relaxation in twisted MoS_2/WS_2 heterobilayers ($\theta = 3.5°$ and $56.5°$) and how the moiré potential and moiré exciton charge density can be affected by the lattice relaxation. The results are included in *SI Appendix*, Figs. S4–S7.

As illustrated above, an important consequence of the cooperation effect is the localization of the excitons. The enhanced exciton localization corresponds to higher exciton binding energies shown in Tables 1 and 2. The strongly localized excitons in Fig. 2 *E*, *F*, *H*, and *I* yield greater binding energies than the weakly localized excitons in Fig. 2 *C*, *D*, and *G*. In particular, the exciton binding difference among A, B, and C can reach over 100 meV in the twisted heterobilayer with $\theta = 3.5°$ and over 140 meV with $\theta = 56.5°$. As strongly bound and localized excitons are preferred in many optoelectronic and quantum information applications, it is of interest to design vdW heterostructures that can host such excitons. Here, we show that defect engineering is a promising approach to accomplish this goal, along with the control of twist angles.

In Fig. 3 *A* and *B*, we present the single-particle band structure for the twisted MoS_2/WS_2 heterobilayer ($\theta = 3.5°$) with S vacancy at the B site of MoS_2 layer and WS_2 layer, respectively. The calculation was based on density functional theory (DFT) with Perdew–Burke–Ernzerhof functional (41). Two sets of flat bands

emerge; the first set results from the defect potential and lies below the CBM, and the second set stems from the moiré potential and is at the VBM. The defect band is nearly flat (doubly degenerate for $S_v@MoS_2$), indicating negligible defect–defect interaction. The bandwidth of the second set is 7 meV, which is identical to that in the defect-free, twisted MoS_2/WS_2 heterobilayer. Thus, this "flat" band results entirely from the moiré potential. Thus, one may view the moiré potential as an artificial defect that traps holes. In contrast to real defects, the moiré potential and the bandwidth can be tuned continuously by the twist angle without changing the material chemistry. We do not include the many-body corrections (e.g., GW) and spin–orbit coupling (SOC) in determining the band structures in Fig. 3 *A* and *B* because they are not expected to have substantial effects on the bandwidths.

We have also examined electron–hole transitions involved in the moiré excitons. As shown below, Φ_I is the many-body wavefunction of the exciton state I, expressed as a linear combination of electron–hole transitions (42). The ground-state wavefunction Φ_0 is taken as a single Slater determinant of occupied Kohn–Sham (KS) orbitals. $a^\dagger_{j\sigma}(a_{i\sigma})$ is the creation (annihilation) operator acting on the jth (ith) KS orbital with spin σ, and $Z_{I,ij}$ represents the corresponding electron–hole transition amplitude (details can be found in *Methods*):

$$\Phi_I \approx \sum_{ij\sigma} Z_{I,ij} a^\dagger_{j\sigma} a_{i\sigma} \Phi_0.$$

In Fig. 3 *C* and *D*, we show the relative contribution of each electron–hole transition to the moiré excitons in the pristine heterobilayer ($\theta = 56.5°$) and the defective bilayer ($S_v@MoS_2@B$). For each exciton, the electron–hole transitions involved are represented by a column of dots and the size of each dot is proportional to the square of the corresponding electron–hole transition amplitude $Z_{I,ij}$. It is found that the dominant contributions to the lowest moiré exciton in the pristine lattice stem from the VBM to CBM and the VBM to CBM+1 transitions, whereas the dominant contribution to the lowest moiré exciton in $S_v@MoS_2@B$ is between the VBM and the defect level (Cd1). As the exciton energy increases, more electron–hole transitions are involved in each exciton. In particular, the low-energy excitons in the defective bilayer comprise primarily the defect levels Cd1 and Cd2, but their contributions diminish or disappear as the energy increases.

Formation of 1D Moiré Excitons via Defect Engineering. Next, we illustrate how the interplay of the two potentials can be tailored via defect engineering to achieve designer exciton lattices, such as 1D moiré excitons. To this end, we introduce S_v at locations away from the high symmetry points. This is possible and even probable because the vacancy formation energy shows little variation within the planes (the energy difference among A, B, and C is less than 20 meV) and the many more available sites would lead to entropy gain.

As shown in Fig. 4 *A–C*, one can generate 1D stripes of moiré excitons in various orientations by defect engineering in MoS_2/WS_2 twisted heterobilayer ($\theta = 56.5°$). When S_v is introduced in MoS_2 layer away from the high symmetry points, the hole is attracted by both the defect potential and the moiré potential (with its minimum at C). As a result, the hole adopts a 1D distribution, turning the exciton lattice from 0D to 1D. The orientation of the 1D stripes, along the direction linking the defect and C, can thus be tailored by the defect position. The 1D moiré exciton lattice can also be formed in the presence of Mo and W vacancies as shown in *SI Appendix*, Fig. S8, showing the robustness of defect engineering. To ensure that the formation of the 1D excitons is not an artifact of the periodic boundary conditions used in the calculations, we also perform the calculations for an isolated defect (S_v) by introducing large vacuum in the supercell. As shown in *SI Appendix*, Fig. S9, the exciton charge density retains the 1D-like distribution across the
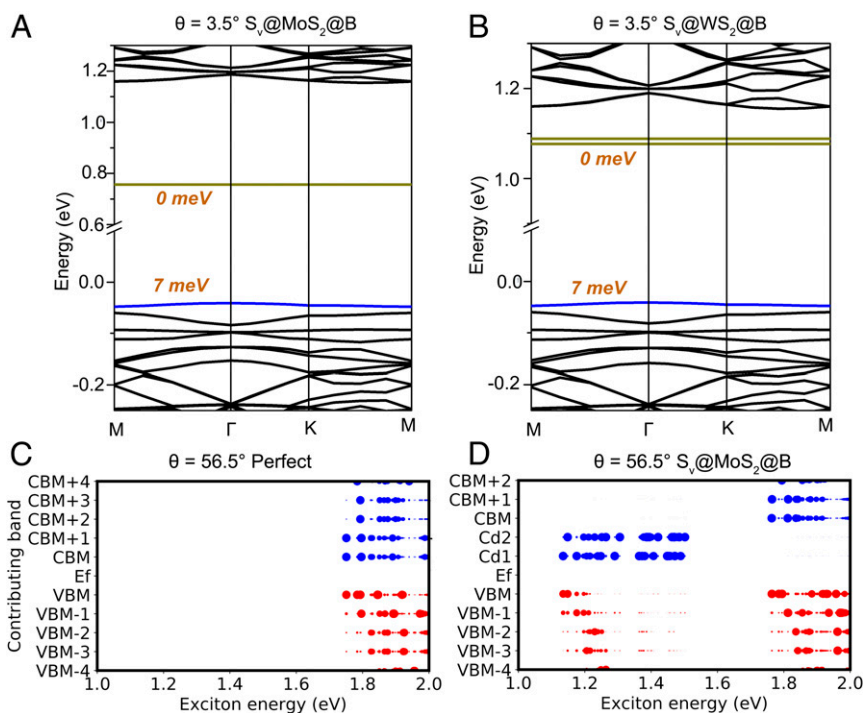
Fig. 3. Single-particle band structure of MoS_2/WS_2 twisted heterobilayer ($\theta = 3.5°$) with a S vacancy at the point B of MoS_2 layer (A) and WS_2 layer (B), respectively. The blue and cyan lines represent the intrinsic VBM and defect levels, respectively. Relative contributions of electron–hole transitions to moiré excitons in the perfect heterobilayer with $\theta = 56.5°$ (C) and the defective bilayer $S_v@MoS_2@B$ (D). Cd1 and Cd2 refer to the (flat) defect levels. The size of the dots is proportional to the square of the electron–hole transition amplitude.

entire supercell. Therefore, we predict that the 1D moiré excitons can emerge at relevant length-scales in TMD bilayers depending on the defect configurations. Although our calculations are based on a defect concentration of 4.18×10^{12} cm^{-2}, we believe the prediction is

valid for a wide range of defect concentrations. Recently, 1D stripes of substitutional defects have been reported in $Mo_xW_{1-x}S_2$ ($x \sim 0.5$) alloys (43), which could lead to the formation of 1D moiré excitons along the stripes. Electron-beam irradiation has also been proposed
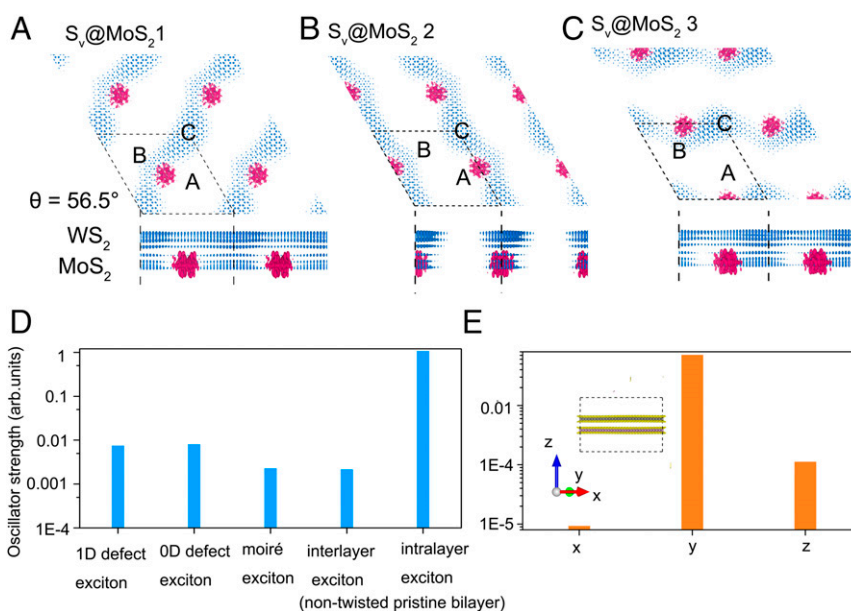

Fig. 4. (A–C) Charge density of the lowest exciton in twisted MoS_2/WS_2 heterobilayer ($\theta = 56.5°$) with a single S vacancy at various sites of MoS_2 layer. Red and blue colors represent the charge densities of electron and hole, respectively. Both top and side views are shown. The unit cell of the moiré superlattice is indicated by the dashed box. All iso-surface value is set at 0.0001 e/Å^3. (D) Oscillator strength of the lowest 1D exciton shown in A, the lowest 0D defect exciton shown in SI Appendix, Fig. S3A, the moiré exciton shown in SI Appendix, Fig. S3A, the lowest interlayer exciton, and the lowest intralayer exciton in the nontwisted pristine bilayer. (E) The x, y, z components of the oscillator strength of the 1D exciton in A, showing a strong anisotropy.

Guo et al.
Moiré excitons in defective van der Waals heterostructures

PNAS | 5 of 9
https://doi.org/10.1073/pnas.2105468118

as a promising approach for engineering defects in TMDs (17), and thus could potentially yield 1D moiré excitons.

Recent experiments (11) reported the formation of 1D moiré potentials in twisted $WSe_2/MoSe_2$ heterobilayers under 8% uniaxial strains. Thus, both defect and strain engineering could yield 1D moiré excitons in twisted TMD heterobilayers. As 1D excitons exhibit drastically different optoelectronic properties from the 0D excitons (11), the defect and strain engineering could open doors for on-demand applications in optoelectronic and quantum computing devices.

To provide additional physical insight, we next compare the oscillator strengths for the five exciton species discussed above, focusing on the lowest energy exciton of each species. They are the 1D defect exciton shown in Fig. 4A, the 0D defect exciton shown in *SI Appendix*, Fig. S3D, the moiré exciton in the pristine bilayer in *SI Appendix*, Fig. S3A, the delocalized interlayer (in Fig. 1B), and the intralayer excitons in the nontwisted pristine bilayer. As displayed in Fig. 4D, although the defect excitons (1D and 0D) have very similar oscillator strengths, the 1D exciton exhibits significant anisotropy (Fig. 4E). The defect excitons have slightly larger oscillator strengths than the moiré exciton in the pristine bilayer. Because the defect excitons and the moiré exciton are of interlayer nature, their oscillator strengths are comparable as that of the interlayer exciton in the nontwisted heterobilayer. However, all four interlayer excitons have much smaller (approximately three orders of magnitude) oscillator strengths than that of the intralayer exciton in the nontwisted heterobilayer. This trend in oscillator strength is consistent with the photoluminescence (PL) measurements in $MoS_2/MoSe_2$ bilayers in which the interlayer exciton PL peak is found to be much weaker than the intralayer exciton peak, and the PL peak of the defect-bound excitons is comparable to that of the interlayer excitons (44). Although the interlayer excitons possess much smaller oscillator strengths, their lifetimes are much longer, which is crucial for the generation of macroscopically ordered excitonic states, such as superfluidity (45) and Bose–Einstein condensation (46, 47). The presence of interlayer dipoles also enables electric tuning of their optoelectronic properties due to the Stark effect. The longer lifetimes combined with the electric controllability render the interlayer moiré excitons particularly promising in applications such as excitonic field-effect transistors at room temperatures (48) and quantum computing (49).

Tuning Excitons by Electric Field. Because the interlayer exciton features an electric dipole that can couple with a perpendicular electric field due to the Stark effect, the position, emission energy, polarity, and hybridization of moiré excitons can be tuned by the electric field (28, 38). As shown in Fig. 5, a positive field, pointing from WS_2 to MoS_2 layer, would increase the energy of MoS_2 and lower the energy of WS_2 and vice versa for a negative electric field. Since the energy levels can be tuned by the electric field, so are the moiré potentials. We have examined how the moiré potential can be modulated by the electric field for both R- and H-stacking structures, and the results are shown in *SI Appendix*, Fig. S10. We find that both the magnitude and the position of the moiré potential extremes can be tuned by the electric field.

When the S_v is in WS_2 layer of twisted WS_2/MoS_2 heterobilayer ($\theta = 3.5°$), the lowest energy exciton (represented by a dashed oval) comprises an electron from the defect level (black) in WS_2 and a hole from VBM in WS_2, depicted in Fig. 5A. Under a positive field, both energies decrease. As a result, the hole could tunnel from WS_2 to MoS_2 as the VBM offset between the two layers diminishes. As illustrated by the exciton charge density with $\bar{S}$ vacancy at A of WS_2, the resonant tunneling of the hole turns the intralayer exciton at E = 0 (Fig. 5A) to an interlayer exciton (Fig. 5C) at E = 0.36 V/nm (see *SI Appendix*, Fig. S11 on how the effective electric field E is estimated). Under a negative field of E = −0.58 V/nm, on the other hand, the defect level is raised above the CBM of MoS_2; thus, the exciton could escape from the defect potential

and recovers its defect-free characteristics, including its position and polarity. Specifically, the electric field drives resonant tunneling of the electron from WS_2 to MoS_2, and thus de-traps the electron from the defect potential. However, the moiré potential remains effective, and the exciton charge density resembles that in the perfect MoS_2/WS_2 twisted heterobilayer under the same field (28). In other words, the negative electric field could de-activate or neutralize the S_v for the excitonic properties.

When the S_v is in MoS_2 layer, the lowest energy exciton consists of an electron from the defect level at MoS_2 and the hole from the VBM of WS_2 (Fig. 5E). In the absence of the electric field, the exciton exhibits a hybrid interlayer and intralayer character thanks to the small VBM band offset between WS_2 and MoS_2. Under a positive field, the VBM offset is further reduced, which promotes hole tunneling from WS_2 to MoS_2, thus increasing the degree of exciton hybridization (Fig. 5G). Under a negative field, the opposite is observed with the hole tunneling back to WS_2 layer and the exciton is trapped more strongly at the defect (Fig. 5H). Hence, compared to the zero field, the negative field deepens both the defect and moiré potentials (28), yielding strongly localized excitons at the defect. The similar phenomena are also observed in twisted WS_2/MoS_2 heterobilayer with $\theta = 56.5°$ (*SI Appendix*, Fig. S12). We thus demonstrated that external means, such as the electric field, can be applied to tune the interplay of the two potentials, which in turn can tailor the optoelectronic properties of twisted TMD heterostructures.

Discussion

In this work, by means of first-principles simulations, we elucidate the interplay—the competition and the cooperation—of the defect and moiré potentials in modulating the excitonic properties of vdW heterostructures. With the twisted MoS_2/WS_2 heterobilayers as examples, we illustrate how the excitonic properties can be tuned by the position and the type of the vacancy defects. When S vacancy is introduced at the high symmetry point B or C in either layer, the two potentials cooperate, leading to more localized excitons at the defects and higher exciton binding energies. When the S vacancy is at point A, on the other hand, the two potentials compete, partially separating the exciton and reducing its binding energy. The interplay of the two potentials is stronger in the twisted MoS_2/WS_2 heterobilayer with $\theta = 56.5°$ than that with $\theta = 3.5°$ and could result significant in-plane variations of exciton binding energy (30–140 meV). In all cases, robust moiré excitons are observed. The interplay of the two potentials can also affect the nature and the degree of hybridization of the excitons. Both the defect and moiré potentials can yield nearly flat bands, whose bandwidth can be tuned by the defect concentration and the moiré superlattice constant. The interplay of the two potentials can be controlled by the vertical electric field. When the S vacancy is in WS_2 layer, the negative electric field reduces the defect potential and de-traps the exciton, which recovers its defect-free characteristics. In contrast, when the defect is in MoS_2 layer, the same electric field deepens the defect and moiré potentials and the exciton becomes more localized at the defect. Last, the interplay of the two potentials can be tailored via defect engineering to create 1D exciton lattices with tunable orientations, and thus open doors for optoelectronic and quantum information applications on-demand.

Methods

First-Principles Ground-State Calculations. The ground-state properties, including single-particle band structures, defect formation energies, and equilibrium geometries of various MoS_2/WS_2 heterobilayers were determined using Vienna Ab initio Simulation Package (50, 51). The Perdew–Burke–Ernzerhof exchange-correlation functional (41) along with projector-augmented wave potentials (52) were employed in these calculations. The vdW interaction was considered via vdW-D2 functional (53). The energy cutoff for the plane-wave basis set was 400 eV. For the band structure calculations, five special k-points were sampled along each of the high symmetry lines in the Brillouin zone. The atomic geometry in each moiré superlattice was fully optimized until the residual force
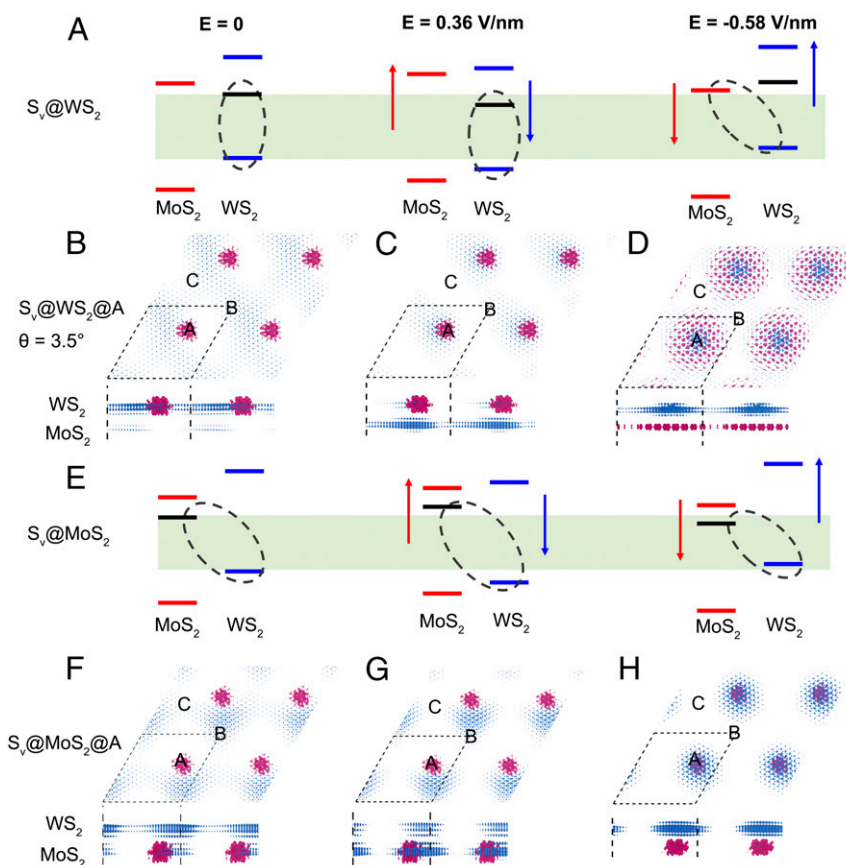
Fig. 5. Electric field tuning of exciton charge density. Type II band alignment in the twisted heterostructure ($\theta = 3.5°$) with S vacancy at point A in WS$_2$ (*A*) or MoS$_2$ (*E*) layer as a function of a vertical electric field E. The energy levels (and the corresponding Stark shift) in MoS$_2$ and WS$_2$ layer are shown by the red and blue lines (and arrow), respectively. The charge density of the lowest exciton with S vacancy at the point A in WS$_2$ (*B–D*) or MoS$_2$ (*F–H*) layer under the different electric fields. Red and blue colors represent the charge densities of electron and hole, respectively. The unit cell of the moiré superlattice is indicated by the dashed box. All iso-surface value is set at 0.0001 e/Å^3.

on each atom was less than 0.01 eV·Å^{-1}. A 20-Å vacuum layer was included to separate the periodic images of MoS$_2$/WS$_2$ slab. The electron densities of the VBM in the pristine MoS$_2$/WS$_2$ heterobilayers (3.5° and 56.5°) agree very well to the scanning tunneling microscope dI/dV mappings of the VBM for the same twist angles in WSe$_2$ homobilayers (54). The lattice relaxation for the pristine and defective MoS$_2$/WS$_2$ heterobilayers (3.5° and 56.5°) is examined and results are discussed in *SI Appendix*, Figs. S4 and S7.

First-Principles Excited-State Calculations. To determine the energies and the many-body wavefunctions of excitons in the moiré superlattices, we employed a recently developed first-principles approach based on the linear-response time-dependent density functional theory (LR-TDDFT) (29, 30) with an optimally tuned, screened and range-separated hybrid exchange-correlation functional (OT-SRSH) (31–35). The OT-SRSH functional is able to reproduce the correct long-range electron–electron and electron–hole interactions in solids by choosing the reasonable parameters. We then solve the following non-Hermitian eigenvalue equations of Casida (55):

$$\begin{pmatrix} A & B \\ B^* & A^* \end{pmatrix}\begin{pmatrix} X_l \\ Y_l \end{pmatrix} = \omega_l \begin{pmatrix} 1 & 0 \\ 0 & -1 \end{pmatrix}\begin{pmatrix} X_l \\ Y_l \end{pmatrix}, \qquad [1]$$

where the pseudoeigenvalue ω_l is the lth exciton energy level. The matrix elements of **A** and **B** in the basis of KS states ($ij\sigma$) are given by the following:

$$A_{ij\sigma,kl\tau} = \delta_{i,k}\delta_{j,l}\delta_{\sigma,\tau}(\varepsilon_{j\sigma} - \varepsilon_{i\sigma}) + K_{ij\sigma,kl\tau}, \qquad [2]$$

$$B_{ij\sigma,kl\tau} = K_{ij\sigma,lk\tau}. \qquad [3]$$

Here, K is the coupling matrix where indices i and k indicate the occupied orbitals, and j and l represent the virtual KS orbitals. According to the assignment ansatz of Casida, the many-body wavefunction of an excited state l can be written as follows:

$$\Phi_l \approx \sum_{ij\sigma} \frac{X_{l,ij\sigma} + Y_{l,ij\sigma}}{\sqrt{\omega_l}} a^\dagger_{j\sigma} a_{i\sigma} \Phi_0 = \sum_{ij\sigma} Z_{l,ij} a^\dagger_{j\sigma} a_{i\sigma} \Phi_0, \qquad [4]$$

where $z_{l,ij} = (X_{l,ij} + Y_{l,ij})/\sqrt{\omega_l}; a_{i\sigma}$ is the annihilation operator acting on the ith KS orbital with spin σ and Φ_0 is the ground-state many-body wave function taken to be the single Slater determinate of the occupied KS orbitals.

In the (TD)DFT-OT-RSH method, there are three parameters, α, β, and γ, that need to be specified. α controls the short-range exact exchange and β is chosen to satisfy the requirement $\alpha + \beta = 1/\varepsilon_0$. The scalar dielectric constant of MoS$_2$/WS$_2$ heterostructure ε_0 was set to 4.0; ε_0 was obtained by averaging the dielectric constants, computed from one-shot GW calculations on a primitive unit cell of MoS$_2$/WS$_2$ heterobilayer, in three directions. The optimal set of the parameters ($\alpha = 0.12$, $\beta = 0.13$, $\gamma = 0.05$) was determined by fitting the quasiparticle gap of MoS$_2$/WS$_2$ heterobilayer from the DFT-OT-RSH calculations to that from the GW calculations. These parameters were found to yield excellent results for the defects as well, as discussed in the main text. The exciton binding energy E_b is defined as the difference between the quasiparticle gap and the optical gap. For the pristine nontwisted MoS$_2$/WS$_2$ heterobilayer, $E_b = 0.37$ eV, which is in line with previous experimental and theoretical reports (56–60). More specifically, the binding energies of the interlayer excitons in nontwisted MoS$_2$/WSe$_2$ and MoSe$_2$/WSe$_2$ bilayers are estimated to be greater than 0.2 eV (57, 58). The exciton binding energy is estimated between 0.36 and 1.55 eV in the nontwisted MoS$_2$/WS$_2$ heterobilayer from an experimental report (56), and their model analysis further reduces the range to 0.4–0.6 eV. The GW-BSE calculations in ref. 60 indicate that the binding energy of the interlayer exciton in nontwisted MoS$_2$/WSe$_2$ bilayer is up to 0.3 eV, and the GW-BSE calculations in ref. 57 show that the interlayer exciton binding energy in MoS$_2$/WS$_2$ bilayer is 0.43 eV, and exciton binding energy in MoSe$_2$/WSe$_2$ bilayer is 0.32 eV. Our results listed in Tables 1 and 2 are also in line with these numbers. Due to the confinement of moiré potentials, there is an energy splitting among low-energy moiré excitons.

Guo et al.
Moiré excitons in defective van der Waals heterostructures

PNAS | 7 of 9
https://doi.org/10.1073/pnas.2105468118

Our TDDFT-OT-RSH calculations predicted an energy spacing of 33 meV among the four lowest-energy excitons, in excellent agreement with the experimental estimate of ~30 meV (39). Owing to the large unit cells (1,626 atoms) in our LR-TDDFT calculations, only the Γ point was sampled in the Brillouin zone. The (TD)DFT-OT-RSH method has been applied to a variety of semiconductors, including graphene fluoride, phosphorene, 2D perovskites, TMD heterostructures, organics, etc. (24–28). More information on the (TD)DFT-OT-RSH method and its validations can be found in these references.

SOC Correction. Owing to high computational cost, we did not include the SOC correction in our large-scale (TD)DFT-OT-RSH calculations, which can be justified in the following. As shown in the previous work, the formation of localized moiré excitons and flat VBM bands in the pristine twisted MoS_2/WS_2 heterobilayers is not affected by the SOC correction (28). To examine whether this conclusion still holds in the presence of defects, we have included the SOC correction in the ground-state calculations of a twisted MoS_2/WS_2 heterobilayer with $\theta = 21.78°$. The larger angle was used here to reduce the computational cost. Two calculations were performed with a S vacancy introduced in either MoS_2 or WS_2 layer using a 3×3×1 supercell. Based on the SOC corrected single-particle energy levels and orbitals, we correct the excited-state energy, following the method proposed in ref. 61:

$$\Delta\Omega^S = \sum_{vc} \left| A_{vc}^S \right|^2 \Delta\varepsilon_{vc}^{SOC}. \tag{5}$$

Here, $\Delta\Omega^S$ represents the energy correction to the sth excited state, which is a linear combination of pairs of valence (v) and conduction (c) bands. A_{vc}^S denotes the expansion coefficient for a given pair of v and c bands. $\Delta\varepsilon_{vc}^{SOC}$ is the SOC corrected energy separation between the v and c bands. The summation is over all pairs of the valence and conduction bands. With S_v in MoS_2 layer, the SOC correction yields negligible change (0.03 eV) to $\Delta\Omega^S$. With S_v in WS_2 layer, a larger change to $\Delta\Omega^S$ (0.18 eV) is obtained for the lowest exciton. However, the main quantity of interest, i.e., the binding energy of the lowest exciton is barely changed (0.01 eV) with S_v in either MoS_2 or WS_2 layer because the SOC correction to the quasiparticle bandgap nearly cancels the correction to the exciton energy (or the optical gap). Furthermore, there is negligible change to the charge densities of the VBM and the defect state with the inclusion of the SOC correction as shown in *SI Appendix*, Fig. S13. Note that the VBM and the defect state are the most relevant states (with a dominant contribution) to the excitonic states as shown in Fig. 3 *C* and *D*. Thus, the exciton charge density is not expected to change substantially with the inclusion of SOC, specially, in terms of the qualitative features discussed in this work.

Data Availability. All study data are included in the article and/or supporting information.

1. Y. Cao *et al.*, Correlated insulator behaviour at half-filling in magic-angle graphene superlattices. *Nature* **556**, 80–84 (2018).
2. Y. Cao *et al.*, Unconventional superconductivity in magic-angle graphene superlattices. *Nature* **556**, 43–50 (2018).
3. C. R. Dean *et al.*, Hofstadter's butterfly and the fractal quantum Hall effect in moiré superlattices. *Nature* **497**, 598–602 (2013).
4. E. C. Regan *et al.*, Mott and generalized Wigner crystal states in WSe₂/WS₂ moiré superlattices. *Nature* **579**, 359–363 (2020).
5. Y. Xu *et al.*, Correlated insulating states at fractional fillings of moiré superlattices. *Nature* **587**, 214–218 (2020).
6. Y. Tang *et al.*, Simulation of Hubbard model physics in WSe₂/WS₂ moiré superlattices. *Nature* **579**, 353–358 (2020).
7. Z. Wang *et al.*, Evidence of high-temperature exciton condensation in two-dimensional atomic double layers. *Nature* **574**, 76–80 (2019).
8. K. L. Seyler *et al.*, Signatures of moiré-trapped valley excitons in MoSe₂/WSe₂ heterobilayers. *Nature* **567**, 66–70 (2019).
9. C. Jin *et al.*, Observation of moiré excitons in WSe₂/WS₂ heterostructure superlattices. *Nature* **567**, 76–80 (2019).
10. E. M. Alexeev *et al.*, Resonantly hybridized excitons in moiré superlattices in van der Waals heterostructures. *Nature* **567**, 81–86 (2019).
11. Y. Bai *et al.*, Excitons in strain-induced one-dimensional moiré potentials at transition metal dichalcogenide heterojunctions. *Nat. Mater.* **19**, 1068–1073 (2020).
12. Y.-M. He *et al.*, Single quantum emitters in monolayer semiconductors. *Nat. Nanotechnol.* **10**, 497–502 (2015).
13. M. Koperski *et al.*, Single photon emitters in exfoliated WSe₂ structures. *Nat. Nanotechnol.* **10**, 503–506 (2015).
14. C. Freysoldt *et al.*, First-principles calculations for point defects in solids. *Rev. Mod. Phys.* **86**, 253 (2014).
15. J. Hong *et al.*, Exploring atomic defects in molybdenum disulphide monolayers. *Nat. Commun.* **6**, 6293 (2015).
16. S. Refaely-Abramson, D. Y. Qiu, S. G. Louie, J. B. Neaton, Defect-induced modification of low-lying excitons and valley selectivity in monolayer transition metal dichalcogenides. *Phys. Rev. Lett.* **121**, 167402 (2018).
17. G. Moody *et al.*, Microsecond valley lifetime of defect-bound excitons in monolayer WSe₂. *Phys. Rev. Lett.* **121**, 057403 (2018).
18. S. Zhang *et al.*, Defect structure of localized excitons in a WSe₂ monolayer. *Phys. Rev. Lett.* **119**, 046101 (2017).
19. V. Carozo *et al.*, Optical identification of sulfur vacancies: Bound excitons at the edges of monolayer tungsten disulfide. *Sci. Adv.* **3**, e1602813 (2017).
20. A. Tartakovskii, Moiré or not. *Nat. Mater.* **19**, 581–582 (2020).
21. M. S. Hybertsen, S. G. Louie, Electron correlation in semiconductors and insulators: Band gaps and quasiparticle energies. *Phys. Rev. B Condens. Matter* **34**, 5390–5413 (1986).
22. L. Hedin, New method for calculating the one-particle Green's function with application to the electron-gas problem. *Phys. Rev.* **139**, A796–A823 (1965).
23. M. Rohlfing, S. G. Louie, Electron-hole excitations in semiconductors and insulators. *Phys. Rev. Lett.* **81**, 2312–2315 (1998).
24. L.-y. Huang, X. Zhang, M. Zhang, G. Lu, Optically inactive defects in monolayer and bilayer phosphorene: A first-principles study. *Phys. Rev. Mater.* **2**, 054003 (2018).
25. Y. Gao, M. Zhang, X. Zhang, G. Lu, Decreasing exciton binding energy in two-dimensional halide perovskites by lead vacancies. *J. Phys. Chem. Lett.* **10**, 3820–3827 (2019).
26. J. Liu *et al.*, Charge separation boosts exciton diffusion in fused ring electron acceptors. *J. Mater. Chem. A Mater. Energy Sustain.* **8**, 23304–23312 (2020).
27. J. Liu, X. Zhang, G. Lu, Excitonic effect drives ultrafast dynamics in van der Waals heterostructures. *Nano Lett.* **20**, 4631–4637 (2020).
28. H. Guo, X. Zhang, G. Lu, Shedding light on moiré excitons: A first-principles perspective. *Sci. Adv.* **6**, eabc5638 (2020).
29. E. K. Gross, W. Kohn, Local density-functional theory of frequency-dependent linear response. *Phys. Rev. Lett.* **55**, 2850–2852 (1985).
30. M. A. Marques, N. T. Maitra, F. M. Nogueira, E. K. Gross, A. Rubio, *Fundamentals of Time-Dependent Density Functional Theory* (Springer Science and Business Media, 2012), vol. 837.
31. S. Refaely-Abramson, M. Jain, S. Sharifzadeh, J. B. Neaton, L. Kronik, Solid-state optical absorption from optimally tuned time-dependent range-separated hybrid density functional theory. *Phys. Rev. B Condens. Matter Mater. Phys.* **92**, 081204 (2015).
32. S. Refaely-Abramson *et al.*, Gap renormalization of molecular crystals from density-functional theory. *Phys. Rev. B Condens. Matter Mater. Phys.* **88**, 081204 (2013).
33. D. Wing *et al.*, Comparing time-dependent density functional theory with many-body perturbation theory for semiconductors: Screened range-separated hybrids and the G W plus Bethe-Salpeter approach. *Phys. Rev. Mater.* **3**, 064603 (2019).
34. S. Refaely-Abramson *et al.*, Quasiparticle spectra from a nonempirical optimally tuned range-separated hybrid density functional. *Phys. Rev. Lett.* **109**, 226405 (2012).
35. L. Kronik, J. B. Neaton, Excited-state properties of molecular solids from first principles. *Annu. Rev. Phys. Chem.* **67**, 587–616 (2016).
36. M. M. Ugeda *et al.*, Giant bandgap renormalization and excitonic effects in a monolayer transition metal dichalcogenide semiconductor. *Nat. Mater.* **13**, 1091–1095 (2014).
37. B. Schuler *et al.*, Large spin-orbit splitting of deep in-gap defect states of engineered sulfur vacancies in monolayer WS₂. *Phys. Rev. Lett.* **123**, 076801 (2019).
38. H. Yu, G.-B. Liu, J. Tang, X. Xu, W. Yao, Moiré excitons: From programmable quantum emitter arrays to spin-orbit-coupled artificial lattices. *Sci. Adv.* **3**, e1701696 (2017).
39. K. Tran *et al.*, Evidence for moiré excitons in van der Waals heterostructures. *Nature* **567**, 71–75 (2019).
40. S. Shabani *et al.*, Deep moiré potentials in twisted transition metal dichalcogenide bilayers. *Nat. Phys.* **17**, 720–725 (2021).
41. J. P. Perdew, K. Burke, M. Ernzerhof, Generalized gradient approximation made simple. *Phys. Rev. Lett.* **77**, 3865–3868 (1996).
42. D. P. Chong, *Recent Advances in Density Functional Methods* (World Scientific Publishing, 1995), part I.
43. A. Azizi *et al.*, Spontaneous formation of atomically thin stripes in transition metal dichalcogenide monolayers. *Nano Lett.* **16**, 6982–6987 (2016).
44. N. Zhang *et al.*, Moiré intralayer excitons in a MoSe₂/MoS₂ heterostructure. *Nano Lett.* **18**, 7651–7657 (2018).
45. M. M. Fogler, L. V. Butov, K. S. Novoselov, High-temperature superfluidity with indirect excitons in van der Waals heterostructures. *Nat. Commun.* **5**, 4555 (2014).
46. L. V. Butov, A. C. Gossard, D. S. Chemla, Macroscopically ordered state in an exciton system. *Nature* **418**, 751–754 (2002).
47. L. V. Butov, C. W. Lai, A. L. Ivanov, A. C. Gossard, D. S. Chemla, Towards Bose-Einstein condensation of excitons in potential traps. *Nature* **417**, 47–52 (2002).
48. D. Unuchek *et al.*, Room-temperature electrical control of exciton flux in a van der Waals heterostructure. *Nature* **560**, 340–344 (2018).
49. C. Jiang *et al.*, Microsecond dark-exciton valley polarization memory in two-dimensional heterostructures. *Nat. Commun.* **9**, 753 (2018).
50. G. Kresse, J. Furthmüller, Efficient iterative schemes for ab initio total-energy calculations using a plane-wave basis set. *Phys. Rev. B Condens. Matter* **54**, 11169–11186 (1996).

51. G. Kresse, J. Furthmüller, Efficiency of ab-initio total energy calculations for metals and semiconductors using a plane-wave basis set. *Comput. Mater. Sci.* **6**, 15–50 (1996).
52. P. E. Blöchl, Projector augmented-wave method. *Phys. Rev. B Condens. Matter* **50**, 17953–17979 (1994).
53. S. Grimme, Semiempirical GGA-type density functional constructed with a long-range dispersion correction. *J. Comput. Chem.* **27**, 1787–1799 (2006).
54. Z. Zhang *et al.*, Flat bands in twisted bilayer transition metal dichalcogenides. *Nat. Phys.* **16**, 1093–1096 (2020).
55. D. P. Chong, *Recent Advances in Density Functional Methods* (World Scientific, 1995), vol. 1.
56. H. Chen *et al.*, Ultrafast formation of interlayer hot excitons in atomically thin MoS_2/WS_2 heterostructures. *Nat. Commun.* **7**, 12512 (2016).
57. E. Torun, H. P. Miranda, A. Molina-Sánchez, L. Wirtz, Interlayer and intralayer excitons in MoS_2/WS_2 and $MoSe_2$/WSe_2 heterobilayers. *Phys. Rev. B* **97**, 245427 (2018).
58. J. Kunstmann *et al.*, Momentum-space indirect interlayer excitons in transition-metal dichalcogenide van der Waals heterostructures. *Nat. Phys.* **14**, 801–805 (2018).
59. N. R. Wilson *et al.*, Determination of band offsets, hybridization, and exciton binding in 2D semiconductor heterostructures. *Sci. Adv.* **3**, e1601832 (2017).
60. S. Latini, K. T. Winther, T. Olsen, K. S. Thygesen, Interlayer excitons and band alignment in MoS_2/hBN/WSe_2 van der Waals heterostructures. *Nano Lett.* **17**, 938–945 (2017).
61. D. Y. Qiu, H. Felipe, S. G. Louie, Screening and many-body effects in two-dimensional crystals: Monolayer MoS_2. *Phys. Rev. B* **93**, 235435 (2016).

APPLIED PHYSICAL SCIENCES

Guo et al.
Moiré excitons in defective van der Waals heterostructures

PNAS | 9 of 9
https://doi.org/10.1073/pnas.2105468118